Nanoscale

Directional Sensing Based on Flexible Aligned Carbon Nanotube Film Nanocomposites

Journal:	*Nanoscale*
Manuscript ID	NR-ART-03-2018-002137.R2
Article Type:	Paper
Date Submitted by the Author:	16-Jul-2018
Complete List of Authors:	Sui, Chao; Rice University, Department of Materials Science and NanoEngineering; Harbin Institute of Technology, Center for Composite Materials and Structures Yang, Yingchao; University of Maine, Department of Mechanical Engineering Headrick, Robert; Rice University, Department of Chemistry Pan, Zixuan; Rice University, Department of Materials Science and NanoEngineering Wu, Jianyang; Xiamen University, Department of physics Zhang, Jing; Rice University, Department of Materials Science and NanoEngineering Jia, Shuai; Rice University, Department of Materials Science and NanoEngineering Li, Xinwei; Rice University, Department of Electrical and Computer Engineering Gao, Weilu; Rice University, Department of Electrical and Computer Engineering Dewey, Oliver; Rice University, Department of Chemistry Wang, Chao; Rice University, Department of Materials Science and NanoEngineering; Harbin Institute of Technology, Center for Composite Materials and Structures He, Xiaodong; Harbin Institute of Technology, National Key Laboratory of Science and Technology on Advanced Composites in Special Environments Kono, Junichiro; Rice University, Electrical and Computer Engineering Pasquali, Matteo; Rice University, Department of Chemistry; Rice University, Chemical and Biomolecular Engineering Lou, Jun; Rice University, Department of Materials Science and NanoEngineering

Directional Sensing Based on Flexible Aligned Carbon Nanotube Film Nanocomposites

Chao Sui[a,b,#], Yingchao Yang[c,#], Robert J. Headrick[d,#], Zixuan Pan[a], Jianyang Wu[f], Jing Zhang[a], Shuai Jia[a], Xinwei Li[g], Weilu Gao[g], Oliver Dewey[d], Chao Wang[a,b,]*, Xiaodong He[b], Junichiro Kono[a,g,h], Matteo Pasquali[d,e], Jun Lou[a,d,]*

[a]Department of Materials Science and NanoEngineering, Rice University, 6100 Main Street, Houston, TX 77005, USA

[b]National Key Laboratory of Science and Technology on Advanced Composites in Special Environments, Harbin Institute of Technology, Harbin 150080, China

[c]Department of Mechanical Engineering, University of Maine, 5711 Boardman Hall, Orono, ME 04469, USA

[d]Department of Chemistry, Rice University, 6100 Main Street, Houston, TX 77005, USA

[e]Department of Chemical and Biomolecular Engineering, Rice University, 6100 Main Street, Houston, TX 77005, USA

[f]Department of Physics, Research Institute for Biomimetics and Soft Matter, Fujian Provincial Key Laboratory for Soft Functional Materials Research, Xiamen University, Xiamen 361005, China

[g]Department of Electrical and Computer Engineering, Rice University

[h]Department of Physics and Astronomy, Rice University

[#]C. Sui, Y.C. Yang, and R. J. Headrick contribute equally.

*Corresponding Email: chaowang@hit.edu.cn; jlou@rice.edu

Abstract

The electrical behaviors under mechanical deformation of an aligned single-walled carbon nanotube (SWCNT) film nanocomposite have been systematically investigated in this work. Electrical signals along CNT axis (ǁ) and perpendicular to CNT axis (⊥) follow a specific pattern, which enables the mechanical motion to be determined by vector analysis of such signals. The unique electrical behaviors of the sandwiched nanocomposites originate from the anisotropic characteristics of the CNT films. By combining *in situ* mechanical investigation with a coarse-grained molecular dynamics simulation, the shearing effect between SWCNTs is found to play a key role in stress-transfer along ǁ direction, resulting in arc-shape cracks, while the peeling effect is dominant along ⊥ direction, leading to unifom SWCNT bar bridging at cracks. The fabricated CNT based sandwiched nanocomposite is believed to have great potential in building flexible all-direction sensors.

1. Introduction

Over the last three decades, carbon nanotubes (CNTs) have been considered as one of the most promising materials, due to their outstanding mechanical,[1, 2] electrical,[3, 4] and thermal properties.[5, 6] In addition to these exceptional properties, CNTs also possess high flexibility, low density, and large aspect ratio, which largely broaden their potential applications. One of the applications is that CNTs have been used to fabricate nanocomposites with exceptional mechanical performances. Two representative methods have been commonly adopted. One is to directly disperse CNTs into matrices including polymer, metals, and ceramics.[7-9] The other is to first synthesize CNT-based hierarchical structures including fibers,[10, 11] films[12, 13] and blocks (e.g., aerogels and foams),[14, 15] and then infiltrate matrix vapor or precursor into the structures to form nanocomposite after certain treatments.[16]

Considering their outstanding electrical conductivity, CNTs could find more applications in building motion sensors and electrical conductors.[17-20] If the CNTs are randomly dispersed into matrix, the connections between CNTs could be cut off by the matrix. As a result, the electron cannot freely transport through the fabricated nanocomposites, leading to poor electrical conductivity. In order to improve electron transport efficiency, great effort has been made, such as increasing density of CNTs in matrix and functionalizing CNT surfaces,[21, 22] while the improvement in electron transport efficiency is still marginal. Recently, CNTs have been fabricated into different hierarchical structures. Among them the CNT films caught our attention due to the unique orientation of all CNTs in the film.[23, 24] The well aligned CNTs can guarantee the continuous electron transport in nanocomposites in certain directions. For example, Peng *et al.*[23] prepared a CNT/polymer composite using highly aligned CNTs. The electrical conductivity of the composite reached 200 S/cm along the axial direction of CNTs. In addition to good electrical conductivity, composites reinforced by aligned CNTs also have anisotropic electrical behaviors.[25-27] So far, anisotropic electrical behaviors of nanocomposite reinforced by CNT films and their potential applications have not been systemically investigated.

In this study, we propose a facile design of nanocomposite reinforced by single-walled CNT (SWCNT) films, where a thin layer of aligned SWCNT film was sandwiched between two layers of elastic polydimethylsiloxane (PDMS) matrix. The anisotropic electrical behaviors under mechanical deformation along different directions relative to SWCNT axis were monitored by an electrical measurement system. In order to correlate mechanical deformation and electrical response of the SWCNT films, *in situ* tensile test of individual SWCNT film and coarse-grained molecular dynamics (CGMD) simulation were carried out. At last, a direction sensor important for artificial skins for robots was designed based on such SWCNT film sandwiched composites.

2. Results and Discussion

The aligned SWCNT film was prepared onto glass slide by a sliding coating method reported previously.[28] The film itself can float on water shown in Fig. 1a, which makes it possible to be transferred onto different kinds of substrates including metals, polymer, and ceramics. To quantify mechanical properties, the SWCNT film is loaded onto a piece of polyethylene terephthalate (PET) with a square hole at the center. The film can freely suspend over the hole without fracture shown in Fig. 1b. Moreover, the thickness of SWCNT films can be controlled between 20 nm and 200 nm (Fig. 1c) by adjusting the concentration of SWCNT in solution and the normal force on the glass slide. Fig. 1d shows an AFM image of the SWCNT film with thickness of ~60 nm. The typical mophological structures of aligned SWCNT film SWCNTs were shown in Fig.s 1e-f. Earlier work indicated that the alignment degree of structure in hierachical materials is related to their multifunctional properties.[29, 30] In this study, we employed the terahertz time-domain spectroscopy (THz-TDS) to quantitatively characterize the alignment degree of SWCNT films. This method has been successfully used for quantitatively studying the anisotropy of SWCNT films.[30] Specifically, through THz-TDS we can obtain the nematic order parameter S for two-dimensional materials according to $S=\frac{A_{\parallel}-A_{\perp}}{A_{\parallel}+A_{\perp}}$, where $A_{\parallel}$ and $A_{\perp}$ are the attenuations along SWCNT axis (∥) and the direction perpendicular to SWCNT axis (⊥) as shown in Fig. 1e, respectively. The parameter S is related to angle distribution followed by $S=< 2\cos^2(\theta) - 1 >$, therefore it can be used to directly describe the degree of SWCNT alignment. The value of S ranges from 0 to 1, where 0 and 1 are corresponding to random distribution and perfect alignment of SWCNTs, respectively. On the one hand, it was found that in our material system $A_{\parallel}$ is stronger than $A_{\perp}$, indicating an obvious anisotropic structure (Fig. 1g). On the other hand, S was calculated to be ~ 0.6 (Fig. 1h).

To fabricate flexible aligned SWCNT film sandwiched nanocomposites, the PDMS elastomer base mixed with curing agent with a proportion of 10:1 was selected as matrix. As shown in Fig. 2a, a layer of PDMS with thickness of ~1.0 mm as bottom layer was spread into a petri dish. The SWCNT film suspended on a polished copper sheet with a hole at the center was gently loaded onto the PDMS followed by dropping another of layer of PDMS with thickness of ~1.0 mm. After 10 min degas, the sandwiched composite was cured at 70° for 1 h in a high vacuum oven. Both ends of Cu were respectively soldered with a flexible conductive wire which was connected to a Keithley analyzer for electrical measurement during mechanical deformation.

Both electrical behaviors along (∥) and (⊥) were carefully monitored. Before loading, the electrical resistances along (∥) and (⊥) were 10 Ω and 38 Ω, respectively. Fig. 2b shows the resistance change under initial tensile loading. Note that R and R_0 are the electrical resistances under and before mechanical loading, respectively, and $(R-R_0)/R_0$ denotes the resistance change. With the increase of strain, the resistance change remains relatively stable until the strain reaches 16% along (∥) and 50% along (⊥) directions. Afterwards, the resistance change increases dramatically. When strain reaches 22% and 80% along both directions, the connection is in open circuit, demonstrating that the SWCNT film completely fractured. This switch-like electrical behavior can also be found in other works.[31, 32] To better correlate electrical behavior and mechanical deformation, selected snapshots at different strains are included in Fig. 2c-d. During tensile testing, a small crack initiated in the SWCNT film at strain of 12% along ∥ direction. With increase of strain, the crack continues growing and several new cracks generate as well. The initial crack was found at strain of 15% along ⊥ direction. Interestingly, the crack evolution under mechanical deformation along two directions is totally different. The cracks, which are in arc-shape along ∥ direction, almost pass through the whole cross section. While the cracks along ⊥ direction, which are shorter and denser, were divided into narrow SWCNT bridge patterns shown in Fig. 2d.[33, 34]

After initial loading and unloading, more cyclic tests were carried out to understand the stability of electrical properties of sandwiched composite. The maximum strain was controlled at 16% and 50% along (∥) and (⊥) directions, respectively. Fig. 2e-f show cyclic behaviors of resistance change as function of strain along both directions. It is found that the electrical resistance after initial cycle loading increased to ~100 Ω along (‖) and ~50 Ω along (⊥), which demonstrates 900% and 25% increase compared to original resistance. The reasons may include: Firstly, although the SWCNTs in the film are mostly well aligned, there are still some SWCNTs crossing each other; these SWCNTs would coordinate with each other in displacements to maintain contacts during mechanical loading, leading to stable electrical resistance after initial loading. Secondly, with large strain exerted onto the SWCNT film, the weakest point might fracture first, resulting in higher initial electrical resistance. On the other hand, it was also found that tensile electrical behaviors under initial loading is different from that under cyclic loadings. This is mainly due to that under initial loading, when the strain reaches some critical value, the cracking occurs and the number of cracks increases with the increase of strain. During the initial unloading, although the SWCNT films seems to recover to initial state because of excellent elasticity of PDMS matrix, the cracks are retained. Interestingly, under following cyclic tests, we observed that the crack propagation almost follows the cracking trajectory in the initial cycle. This can lead to differences in the number and size of cracks at same strain, therefore the resistance response is also different.

Because the number of cracks during cyclic tests would not change much after the initial loading, the SWCNT films have shown a cyclic stability in electrical resistance. Interestingly, the resistance change along (‖) direction with the increase of strain shown in Fig. 2e is nearly linear and reversible in the cycle tests. While the resistance change is insensitive to the mechanical deformation along (⊥) direction (Fig. 2f). Here we employed the gauge factor (GF) γ calculated as the slopes of resistacne change versus strain curves to further study the electrical sensitivity and anisotropy of our sensor system. The GF along (∥) and (⊥) directions were obtained to be ~59 and ~1, respectively. We compared the sensitivity of our sensor with that of other strain/force sensors assembled by alignment structures as shown in Table 1.[20, 35-39] One can clearly see that our material system can achieve relatively high sensitivity. On the other hand, the sensitivity along (∥) direction is generally much higher than that along (⊥) direction.

To further understand the anisotropy of electrical behaviors, the optical images of the nanocomposite at different strains were captured and demonstrated in Fig. 2g-h. As expected, the number of cracks as well as crack shape resulting from initial loading have no obvious change during cyclic loading, accounting for the stability of electrical response. It is believed that the contact of SWCNTs at cracks plays a key role in the electrical conductivity. Along (∥) direction, the effective contact at cracks depends on the gap width which is strongly corresponding to the mechanical deformation. While along (⊥) direction, the gaps were continuously linked by the SWCNT bridges which largely preserved the contact region. Therefore, the change of electrical resistance under current cyclic loading conditions along (⊥) direction is trivial. As shown in Fig. 2i in more details, along (∥) direction the large resistance change can be mainly attributed to a shearing-sliding mechanism induced by shear stress between CNTs at cracks, where the contact area between CNTs is very sensitive to the crack width. Therefore, although there is no obvious change in the number and morphology of cracks, the slight change of strain relating to crack width could result in large change of resistance. In contrast, along (⊥) direction a peeling effect will dominate the deformation, by which the bridging gaps can be formed. However, with this crack pattern, the change of gap width has less effect on effective contact area between CNTs. Therefore, the electrical response is insensitive to the strain state. The deformation mechanisms of SWCNT films will be further clarified later by the coarse-grained molecular dynamics (MD) simulation.

In order to reveal the origin of electrical anisotropy of sandwiched composite under mechanical deformation, it is essential to understand the structure-mechanical behavior relationship of the film itself. Recently, we developed an effective transfer method and quantified mechanical properties of monolayer two dimensional materials including graphene and $MoSe_2$.[40, 41] All these tests were carried out in a scanning electron microscope (SEM), which enables direct observation of fracture behaviors of the materials. Here, we took advantage of our *in situ* mechanical test capability to study an individual SWCNT film. The SWCNT film was first transferred onto micromechanical device following the transfer procedure developed earlier.[41] The larger contact area between the film and the micromechanical device can provide enough adhesion force to prevent sliding during mechanical tests. As shown in Fig. 3, the width of the suspended SWCNT film is ~ 8 μm. To make sure that the fracture behaviors are comparable, all tested samples were from the same batch of the film. It is found that the fracture behaviors and mechanical properties of SWCNT films along two orthogonal directions are totally different (Fig. 3a-d). The crack path along (||) direction is close to zig-zag shape, while the crack path along (⊥) direction is straight. All crack paths are highlighted using dash line in Fig. 3b and Fig. 3d. Fig. 3e demonstrates representative stress-strain curves along two directions. It was noted that the crack modes of SWCNT films along two direcions are consistent with that in electrical test. The tensile stress σ was calculated by $\sigma=F/wt$, where F is the tensile force, w and t are the width and thickness of samples, respectively. And the tensile strain ε was calculated by $\varepsilon=(L-L_0)/L_0$, where L is the total length of suspended region of SWCNT film after tension and L_0 is the initial length. It can be seen that the σ-ε curves along two directions are linear, indicating that the film is brittle. The mechanical properties of the SWCNT films are summarized in Fig. 3f. The average tensile strength along (||) direction is 765 MPa, which is 284 % larger than that (199 MPa) along (⊥) direction. The average Young's modulus along (||) direction is 126 GPa, demonstrating 448% improvement comparing with that (23 GPa) along (⊥) direction. Meanwhile, the maximum tensile strain along (||) direction is about twice as large as that along (⊥) direction. This in turn would strongly dictate the anisotropic electrical behaviors of the sandwiched composites observed earlier.

To further understand the structural and electrical anisotropy of SWCNT films, we performed a large-scale coarse-grained MD simulation (CGMD) to study the microstructural evolvements of SWCNT films subjected to uniaxial tensile loading. So far, this theoretical method has been widely applied to study various aspects of SWCNT-based materials, such as tensile, compressive and frictional properties, etc.[42,

[43] By using this method, the individual SWCNTs can be described by continuous bead-like microwires. In each SWCNT, the elongating energy contributed by two bonded beads are expressed by $E_{\mathrm{Bond}} = k_{\mathrm{Bond}}(l\text{-}l_0)/2$, where k_{Bond} is the bond stiffness, while l is the spring length between two bonded beads with l_0=1 nm as its equilibrium length. The bending energy contributed by adjacent bead triplets are defined by $E_{\mathrm{Bend}}=k_{\mathrm{Bend}}(\theta\text{-}\theta_0)/2$, where k_{Bend} is the angular spring stiffness and θ is the angle between neighboring springs with θ_0 =180° as its equilibrated angle. Moreover, long-range interactions between discrete beads through van der Waals (vdW) forces are defined by a standard Lennard-Jones expression $E_{\mathrm{pair}}= 4\varepsilon[(\sigma/r)^{12}\text{-} (\sigma/r)^6]$, where σ, ε and r are the distance parameter, the energy well depth at equilibrium and the distance between two interacting beads, respectively. The relevant parameters can be found in the literature.[44] In this study, the well-alignment of SWCNTs, as a baseline model similar to experimental samples, was generated by randomly overlapping sidewalls of equivalent SWCNTs with the same length. The initial generated SWCNT film has dimensions of $1.40\times1.00\times0.30$ μm^3. The whole system is composed of 380110 beads. Planar periodic boundary conditions parallel to the surface was applied (see detailed modeling process in the Experimental Section).

The snapshots of sample structures at four different strains along both orthogonal directions were captured as shown in Fig. 4a-b, in which beads are colored according to corresponding potential energy. It is found that, the shearing effect between side-walls of SWCNTs plays critical role in stress-transfer along (||) direction, whereas the peeling effect is dominant along (⊥) direction. Some experimental and theoretical work has proved that the shearing effect of SWCNTs and other substrates is stronger than peeling effect based on vdW interaction.[45, 46] The main reason is that the effective vdW interaction area based on shearing effect is much larger than that based on peeling effect, thereby resulting in more efficient shearing stress-transfer. It is observed that this shearing effect could induce sliding failure between SWCNTs when the tensile strain reaches 5% as shown in the insets of Fig. 4a. In this case, the propagation of initial cracks along the transverse direction need to overcome the sliding along the loading direction, thereby resulting an uneven crack surface as shown in Fig. 2c and Fig. 3b. For the peeling effect, it can lead to an obvious detaching failure between SWCNTs when strain is at 60%, by which the SWCNT bars were formed and bridged at the cracks (Fig. 4b). This is in agreement with that observed in experiment (Fig. 2d) and correlate well with the anisotropic electrical behaviors under mechanical deformation.

Besides the sidewall contacts between SWCNTs in aligned SWCNT-based structures, the entanglement among SWCNTs also play a key role in the stress-transfer. In our study, we also considered the effect of this entanglement in structural evolution under tension. In actual material system, the morphology of entanglement is very complex. To simplify the model, a self-folding entanglement of two individual SWCNTs described by Lu and Chou[47] was used to establish the aligned SWCNT film (Fig. S1). As shown in Fig. S1a-b, it is found that, the stress can be transferred by an interlocking effect of self-folding entanglements along ($\parallel$) direction, thereby enhancing the load carrying capacity. However, along ($\perp$) direction, this entanglement plays a secondary role in stress-transfer. To further support this viewpoint, we tracked a representative element of SWCNT entanglement colored by potential energy with different tensile strains as shown in Fig. S1c-d. It can be seen that, at same strain interlocking region in entanglement along (‖) direction possesses higher potential energy compared with that along (⊥) direction, indicating a higher stress-transfer efficiency.

Due to the unique anisotropic electro-mechanical behaviors, SWCNT film composites could find more application in direction sensing area, a much needed capability for artificial skins on medical robots. Here we propose and demonstrate such applications shown in Fig. 5a. Although the CNT-based strain sensors have been designed to monitor complex human motion including tension, compression, and bending,[35, 48, 49] the work on detection of direction of external forces is still lacking. Some work indicated that the structural design of cross-shape can make the sensor sensing the direcions.[37, 50, 51] Based on this idea, here a cross-like laminated structure composed of two aligned SWCNT films and PDMS matrix was designed and fabricated as one sensor unit (Fig. 5b). The alignment of CNTs is parallel to the longest side of the film. To guarantee that the electrical signals do not interfere with each other, a small matrix gap between two aligned SWCNT films was intentionally preserved (Fig. 5c). Two aligned SWCNT films were numbered as #1 and #2 (Fig. 5d). The full direction (0°-360°) can be divided into four quadrants and each quadrant covers a 90° domain. The angle between alignment of CNTs and loading direction is set as θ. To unveil the stability of the designed motion sensor, cyclic tests were carried out. Fig. 5e shows the resistacne responses of CNT film #1 and #2 with different angles of θ, where the dependence of resistance change on the strain which first increases from 0 to 5% and then decreases back to 0% followed by another increase to 10%. Meanwhile, it was observed that the resistance change is relatively large within the range of 30°, but tends to be gentle when θ>30°. As shown in Fig. 5f, this can be mainly attributed to the fact that, the loading along angle θ (0°<θ<90°) could lead to a combined shearing and peeling effect on the CNT films. When θ<30°, well-alignment structure can be observed, indicating that the shearing effect predominates the deformation of CNT films and could result in a sliding failure between CNTs. This kind of crack pattern can cause a dramatical change of contact area between CNTs, therefore attaining a good electrical response to strain. When θ>30°, it was observed that the peeling effect prdominate the interaction between CNTs, and result in a bridging/network structure. By this crack pattern, the connection between CNTs is relatively good during loading, which makes the CNT films to show relatively weak electrical response. In practical applications, we can combine the reversed electrical responses of #1 and #2 to monitor arbitrary directions. Such simple design could be used to monitor the force directions, that would find more applications in building more sensitive robots.

3. Conclusion

We fabricated a sandwich composite with aligned CNT film and PDMS and subsequently focused on its electro-mechanical behaviors. The electrical conductivity of this composite is sensitive to tensile strain along || direction, while it is more stable along ⊥ direction. The interface interaction between two CNTs plays an important role in electrical conductivity of CNT films and composites. Along ∥ direction, the shearing dominates the interface, while peeling control the contact along ⊥ direction. This study provides a better understanding on electro-mechanical behaviors of CNT film based sandwich composites and a facile route for building direction sensitive skin sensors.

4. Experimental Section

4.1. Fabrication of SWCNT films

Films were prepared following a preciously reported procedure. Briefly, SWCNTs (EC1.5, Meijo NanoCarbon) were mixed into chlorosulfuric acid (CSA) with concentration of 3.5 mg/mL and mixed with a Flak Tek mixer. The viscous solution was pipetted and sandwiched between two acetone cleaned glass microscope slides which were slid away in opposite direction to align SWCNTs on both slides. The CNTs coated slides were dropped into diethyl ether (Sigma Aldrich) to remove the CSA followed by acetone, ethanol, and water wash several times.

4.2. Fabrication of sandwiched CNT film/PDMS nanocomposite

The PDMS was made of silicone elastomer base (Sylgard 184) and curing agent (Sylgard 184) with proportion of 10:1. A layer of PDMS with thickness of ~1.0 mm was spread into a petri dish. A layer of SWCNT film sitting on a hollow polished copper foil was gently put onto the PDMS followed by dropping another of layer of PDMS with thickness of ~ 1.0 mm. After 10 min degas, the sandwiched composite was cured at 70° for 1 h in high vacuum oven. Both ends of Cu was respectively soldered to a flexible conductive wire which was then connected to a Keithley analyzer for electrical measurements during mechanical deformation.

4.3. Electromechanical measurement

A micromechanical tester equipped with a 200N load cell (Gatan Deben) was employed to carry out uniaxial tensile tests. The loading speed was set as 2 mm/min. Both electrodes were connected to a Keithley analyzer in order to monitor resistance change with mechanical deformation (Fig. S2).

4.4. In situ tensile test of SWCNT film

A thin layer of poly (methyl methacrylate) (PMMA) was first coated over SWCNT sitting on a SiO_2/Si substrate. The SiO_2/Si wafer together with PMMA/CNT film was slowly dropped into NaOH solution to etch off SiO_2 in order to free PMMA/CNT film. A piece of clean polished Cu sheet was used to fish out the PMMA/CNT film followed by washing in deionized water three times. A fine tungsten probe installed in a micromanipulator was employed to cut the PMMA/CNT film out of the entire film and gently loaded onto the nanomechanical device. To obtain the freestanding CNT film, the whole device together with PMMA/CNT film was pushed into a tube furnace (Lindbergh/Blue M^{TM}, Thermo Scientific) under continuous flow of a mixture of 90% N_2 and 10% H_2 at 200 sccm to paralyze PMMA. After paralysis of PMMA, the CNT film was shaped into rectangle by focused ion beam (FIB) in a SEM (FEI, Helios 660) using the minimum beam current, 1 pA (Fig. S3). The sample-loaded nanomechanical device was subsequently glued to a SEM sample stub using a commercial wax which melts at 50 ˚C and solidifies at room temperature. In case of charging, the silver paste

(Ted Pella, Inc) was used to bridge the nanomechanical device and the stub. A quantitative Agilent nanoindenter was used to actuate the device and also measure the load and displacement independently. The tensile testing was monitored through SEM for ensuring the validity of tests as well as visualizing the deformation and fracture processes.

4.5. CGMD simulation

Prior to uniaxial loading, all the beads were quasi-statically relaxed to a local minimum energy configuration under the conjugate gradient method with an energy tolerance of 1.0×10^{-4} eV and a force tolerance of 1.0×10^{-4} eV/Å. The CGMD simulation was run for 1ns under NVT ensemble at high temperature of 1000 K controlled by Nosé-Hoover thermostat to allow the structure to fully relax. The system was subsequently cooled down from 1000 to 298 K at a rate of around 0.97 K/ps with zero external pressure under NPT ensemble using the Nosé-Hoover thermostat and barostat. Finally, a relaxation of 5 ns was conducted under NPT ensembles at 298 K and zero pressure to obtain final model for simulation of mechanical loading. The velocity-Verlet integration algorithm was utilized to integrate the equations with a timestep of 10 fs.

In the part of mechanical loading, the uniaxial loadings were carried out by the deformation control technique under NPT ensemble. During the tensile loading process, the pressure in the other planar direction was controlled to be zero by Nosé-Hoover barostat. This allows model structure to experience expansion/contraction in the transverse directions as a result of the Poisson's effect. A reasonable strain rate of $1.0\times10^{7}\ \mathrm{s}^{-1}$ was chosen. The stress per bead was calculated based on the virial definition of stress using the forces on the beads collected during the CGMD simulation. All calculations were carried out by using the Large-scale Atomic-Molecular Massively Parallel Simulator (LAMMPS) software package.

Acknowledgements

The authors gratefully acknowledge the financial support by the US Department of Energy, Office of Basic Energy Sciences under Grant number DE-SC0018193 and the Welch Foundation (grant C-1716). This work was also financially supported by the National Natural Science Foundation of China (NSFC, Grant No. 51702064, 11502221, 11402065). C. W thanks support of China Scholarship Council (CSC).

References

1. M.-F. Yu, O. Lourie, M. J. Dyer, K. Moloni, T. F. Kelly and R. S. Ruoff, *Science*, 2000, **287**, 637-640.
2. M. S. Wang, D. Golberg and Y. Bando, *Advanced Materials*, 2010, **22**, 4071-4075.
3. P. G. Collins, K. Bradley, M. Ishigami and d. A. Zettl, *science*, 2000, **287**, 1801-1804.
4. A. Lekawa-Raus, J. Patmore, L. Kurzepa, J. Bulmer and K. Koziol, *Advanced Functional Materials*, 2014, **24**, 3661-3682.
5. S. Kaur, N. Raravikar, B. A. Helms, R. Prasher and D. F. Ogletree, *Nature communications*, 2014, **5**, 3082.

6. Y. Song, S. Zhou, K. Jin, J. Qiao, D. Li, C. Xu, D. Hu, J. Di, M. Li and Z. Zhang, *Nanoscale*, 2018, **10**, 4077-4084.
7. J. Suhr, N. Koratkar, P. Keblinski and P. Ajayan, *Nature materials*, 2005, **4**, 134.
8. P. M. Ajayan and J. M. Tour, *Nature*, 2007, **447**, 1066.
9. R. Gottlieb, S. Poges, C. Monteleone, S. L. Suib, A. Tiwari, R. A. Gerhardt and M. Szutkowska, *Advanced Ceramic Materials*, 2016, 146-199.
10. O.-K. Park, H. Choi, H. Jeong, Y. Jung, J. Yu, J. K. Lee, J. Y. Hwang, S. M. Kim, Y. Jeong and C. R. Park, *Carbon*, 2017, **118**, 413-421.
11. Y.-L. Li, I. A. Kinloch and A. H. Windle, *Science*, 2004, **304**, 276-278.
12. B. J. Hinds, N. Chopra, T. Rantell, R. Andrews, V. Gavalas and L. G. Bachas, *Science*, 2004, **303**, 62-65.
13. C. Yu, C. Masarapu, J. Rong, B. Wei and H. Jiang, *Advanced Materials*, 2009, **21**, 4793-4797.
14. M. B. Bryning, D. E. Milkie, M. F. Islam, L. A. Hough, J. M. Kikkawa and A. G. Yodh, *Advanced Materials*, 2007, **19**, 661-664.
15. J. Zou, J. Liu, A. S. Karakoti, A. Kumar, D. Joung, Q. Li, S. I. Khondaker, S. Seal and L. Zhai, *Acs Nano*, 2010, **4**, 7293-7302.
16. K. Li, Y. Yang, Z. Gu, J. Y. Howe, G. Eres, L. Zhang, X. Li and Z. Pan, *Advanced Engineering Materials*, 2014, **16**, 161-166.
17. S. Park, M. Vosguerichian and Z. Bao, *Nanoscale*, 2013, **5**, 1727-1752.

18. O. A. Bârsan, G. G. Hoffmann, L. G. van der Ven and G. de With, *Advanced Functional Materials*, 2016, **26**, 4377-4385.

19. Y. Zhang, C. J. Sheehan, J. Zhai, G. Zou, H. Luo, J. Xiong, Y. Zhu and Q. Jia, *Advanced Materials*, 2010, **22**, 3027-3031.

20. H. Zhao, Y. Zhang, P. D. Bradford, Q. Zhou, Q. Jia, F.-G. Yuan and Y. Zhu, *Nanotechnology*, 2010, **21**, 305502.

21. E. Kymakis and G. A. Amaratunga, *Journal of applied physics*, 2006, **99**, 084302.

22. N. Hu, Y. Karube, M. Arai, T. Watanabe, C. Yan, Y. Li, Y. Liu and H. Fukunaga, *Carbon*, 2010, **48**, 680-687.

23. H. Peng, *Journal of the American Chemical Society*, 2008, **130**, 42-43.

24. V. I. Artyukhov, M. Liu and B. I. Yakobson, *Nano letters*, 2014, **14**, 4224-4229.

25. J. Yang, R. Downes, A. Schrand, J. G. Park, R. Liang and C. Xu, *Scripta Materialia*, 2016, **124**, 21-25.

26. X. Wang, Y. Liu, G. Yu, C. Xu, J. Zhang and D. Zhu, *The Journal of Physical Chemistry B*, 2001, **105**, 9422-9425.

27. T. Prasse, J.-Y. Cavaille and W. Bauhofer, *Composites Science and Technology*, 2003, **63**, 1835-1841.

28. R. J. Headrick, D. E. Tsentalovich, J. Berdegué, E. A. Bengio, L. Liberman, O. Kleinerman, M. S. Lucas, Y. Talmon and M. Pasquali, *Advanced Materials*, 2018, **30**, 1704482.

29. X. Lin, X. Shen, Q. Zheng, N. Yousefi, L. Ye, Y.-W. Mai and J.-K. Kim, *ACS nano*, 2012, **6**, 10708-10719.

30. L. Ren, C. L. Pint, L. G. Booshehri, W. D. Rice, X. Wang, D. J. Hilton, K. Takeya, I. Kawayama, M. Tonouchi, R. H. Hauge and J. Kono, *Nano letters*, 2009, **9**, 2610-2613.

31. C. Yan, J. Wang, W. Kang, M. Cui, X. Wang, C. Y. Foo, K. J. Chee and P. S. Lee, *Advanced materials*, 2014, **26**, 2022-2027.

32. Q. Zheng, X. Liu, H. Xu, M.-S. Cheung, Y.-W. Choi, H.-C. Huang, H.-Y. Lei, X. Shen, Z. Wang and Y. Wu, *Nanoscale Horizons*, 2018, **3**, 35-44.

33. M. K. Blees, A. W. Barnard, P. A. Rose, S. P. Roberts, K. L. McGill, P. Y. Huang, A. R. Ruyack, J. W. Kevek, B. Kobrin and D. A. Muller, *Nature*, 2015, **524**, 204.

34. P. Z. Hanakata, Z. Qi, D. K. Campbell and H. S. Park, *Nanoscale*, 2016, **8**, 458-463.

35. T. Yamada, Y. Hayamizu, Y. Yamamoto, Y. Yomogida, A. Izadi-Najafabadi, D. N. Futaba and K. Hata, *Nature nanotechnology*, 2011, **6**, 296.

36. C. Wang, X. Li, E. Gao, M. Jian, K. Xia, Q. Wang, Z. Xu, T. Ren and Y. Zhang, *Advanced materials*, 2016, **28**, 6640-6648.

37. S. Ryu, P. Lee, J. B. Chou, R. Xu, R. Zhao, A. J. Hart and S.-G. Kim, *ACS nano*, 2015, **9**, 5929-5936.

38. A. Oliva-Avilés, F. Avilés and V. Sosa, *Carbon*, 2011, **49**, 2989-2997.

39. J.-I. Lee, S. Pyo, M.-O. Kim and J. Kim, *Nanotechnology*, 2018, **29**, 055501.

40. P. Zhang, L. Ma, F. Fan, Z. Zeng, C. Peng, P. E. Loya, Z. Liu, Y. Gong, J. Zhang and X. Zhang, *Nature communications*, 2014, **5**, 3782.

41. Y. Yang, X. Li, M. Wen, E. Hacopian, W. Chen, Y. Gong, J. Zhang, B. Li, W. Zhou and P. M. Ajayan, *Advanced Materials*, 2017, **29**, 1604201.

42. C. Wang, B. Xie, Y. Liu and Z. Xu, *ACS Macro Letters*, 2012, **1**, 1176-1179.

43. X. Liu, Q. S. Yang, K. M. Liew and X. Q. He, *Carbon*, 2017, **115**, 220-228.

44. S. W. Cranford and M. J. Buehler, *Nanotechnology*, 2010, **21**, 265706.

45. L. Qu, L. Dai, M. Stone, Z. Xia and Z. L. Wang, *Science*, 2008, **322**, 238-242.

46. C. Sui, Q. Luo, X. He, L. Tong, K. Zhang, Y. Zhang, Y. Zhang, J. Wu and C. Wang, *Carbon*, 2016, **107**, 651-657.

47. W. Lu and T.-W. Chou, *Journal of the Mechanics and Physics of Solids*, 2011, **59**, 511-524.

48. D. J. Lipomi, M. Vosgueritchian, B. C. Tee, S. L. Hellstrom, J. A. Lee, C. H. Fox and Z. Bao, *Nature nanotechnology*, 2011, **6**, 788.

49. Y. J. Jung, S. Kar, S. Talapatra, C. Soldano, G. Viswanathan, X. Li, Z. Yao, F. S. Ou, A. Avadhanula and R. Vajtai, *Nano letters*, 2006, **6**, 413-418.

50. H. Chen, Z. Su, Y. Song, X. Cheng, X. Chen, B. Meng, Z. Song, D. Chen and H. Zhang, *Advanced Functional Materials*, 2017, **27**, 1604434.

51. S.-H. Ha, S.-H. Ha, M.-B. Jeon, J. H. Cho and J.-M. Kim, *Nanoscale*, 2018, **10**, 5105-5113.

Table 1. Sensitivity comparasion of present sensor system to other carbon-based sensors.

Materials	Sensitivity		Ref.
	(∥) direction	(⊥) direction	
Aligned SWCNT film/PDMS nanocomposite	59	1	This work
Aligned SWCNT/PDMS nanocomposite	-[a]	0.82	[35]
CNT yarn	0.38	0.02-0.04	[20]
Carbonized silk fabric/ecoflex nanocomposite	375.2	20.4	[36][b]
Aligned CNT fiber/ecoflex nanocomposite	106	-	[37]
Aligned multi-walled CNT/polysulfone composite films	2.78	-	[38]
CNT arrays	15.05	0.66	[39][c]

[a] the related data was not shown in the referece.

[b] the *x* and *y* directions in the reference were definded as (∥) and (⊥) directions in this work.

[c] the sensitivity of force sensor in the reference was calculated by ratio of resistance change and force change.

Figure captions

Fig. 1. Characterizations of SWCNT films. a) SWCNT film floats on water. b) SWCNT film suspends on PET substrate. c) SWCNT films with different thicknesses are fabricated on glass slides. d) AFM image of the SWCNT film with thickness measurement, where the inset is the thickness curve along black dash line. e) SEM image for aligned SWCNT film. f) TEM image for locally aligned SWCNT film, where the inset demonstrates single-wall structure of used CNTs. (g) THz attenuation spectra of aligned SWCNT film along (∥) and (⊥), respectively. (h) The calculated corresponding nematic order parameter.

Fig. 2. Preparation, electrical and mechanical properties of SRFC. a) Schematic for preparing SWCNT film composites. b) Relationship of electrical resistance and strain along two orthogonal

directions under initial loading. c-d) Tensile snapshots of samples at different strains under initial loading. e-f) Relationship of electrical resistance and strain along two orthogonal directions under cyclic loading. g-h) Tensile snapshots of samples at different strains under 4th loading cycle. (i) Schematic for the formation of crakcs and effect mechanisms on resistance responses along (ǁ) and (⊥) directions.

Fig. 3. In situ tension of SWCNT films. a) Schematic for in situ tensile testing along ǁ direction, where ǁ means that the tensile direction is parallel to axial direction of CNTs. b) SEM images for SWCNT films before and after loading along ǁ direction. c) Schematic for in situ tensile testing along ⊥ direction, where ⊥ means that the tensile direction is perpendicular to axial direction of CNTs. d) SEM images for SWCNT films before and after loading along ⊥ direction. e) Tensile stress-strain curves of a SWCNT film along ǁ and ⊥ directions. f) Comparison of tensile strength and young's modulus along two directions.

Fig. 4. CGMD simulations of SWCNT films along two directions under tensile loading. a) Structural evolvement of SWCNT film along ǁ direction. Strain-induced sliding failure was clearly identified by tracking the target sidewall contact between as shown in the insets. b) Structural evolvement of SWCNT film along ⊥ direction. The peeling failure can result in a bridging at cracks.

Fig. 5. Direction-sensitive artificial skins for robots. a) A schematic for a robot arm, where a piece of artificial skin was covered on the arm of a robot. b) Schematic of direction-sensitive artificial

skins. c) Schematic top and side views of a cross-like laminated structure assembled by two aligned SWCNT films. d) Image of a piece of prepared direction-sensitive artificial skin. e) Response of electrical signal to loading and unloading with different strains. f) Images of samples under the tensile loading along different angle θ.

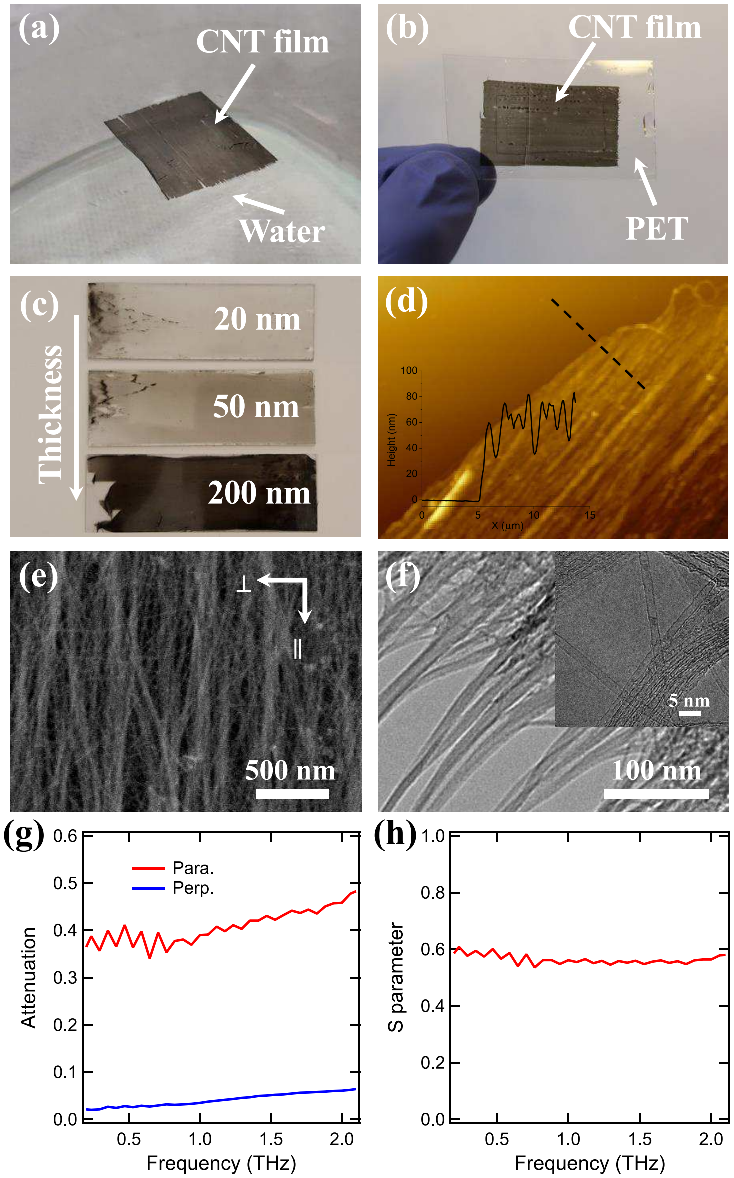

Fig. 1. Characterizations of SWCNT films. a) SWCNT film floats on water. b) SWCNT film suspends on PET substrate. c) SWCNT films with different thicknesses are fabricated on glass slides. d) AFM image of the SWCNT film with thickness measurement, where the inset is the thickness curve along black dash line. e) SEM image for aligned SWCNT film. f) TEM image for locally aligned SWCNT film, where the inset demonstrates single-wall structure of used CNTs. (g) THz attenuation spectra of aligned SWCNT film along (∥) and (⊥), respectively. (h) The calculated corresponding nematic order parameter.

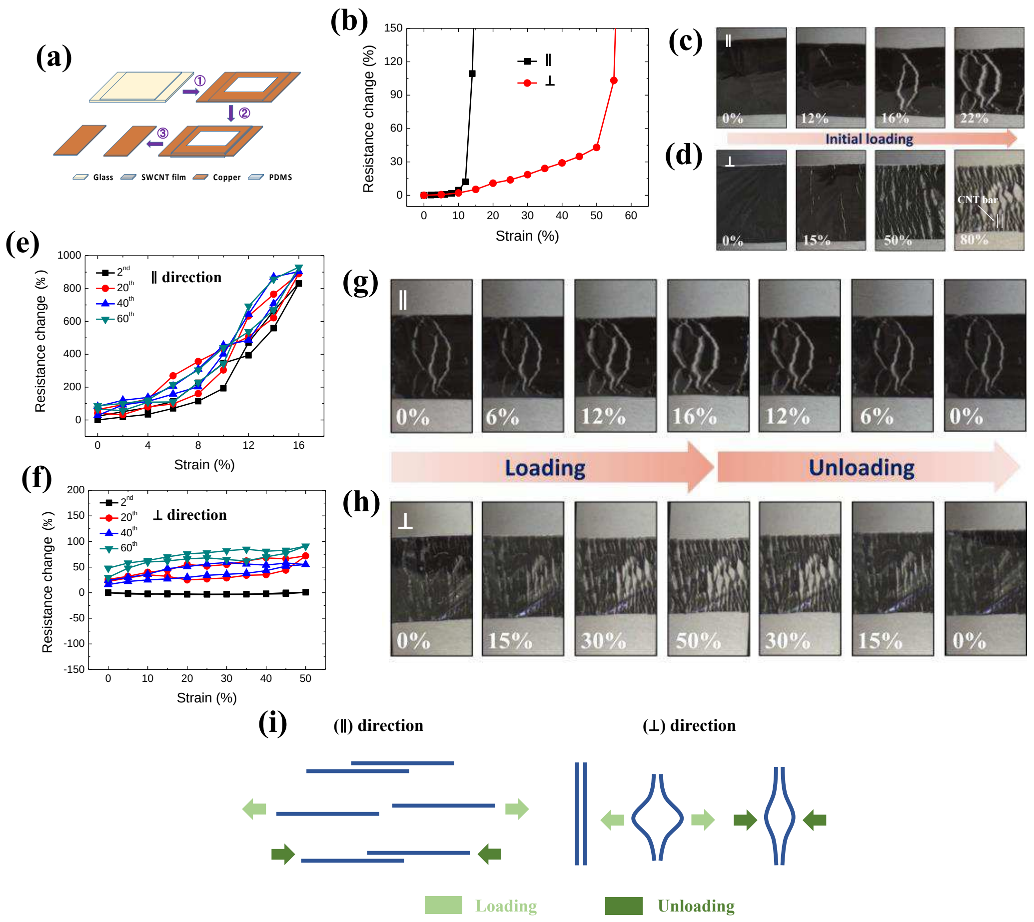

Fig. 2. Preparation, electrical and mechanical properties of SRFC. a) Schematic for preparing SWCNT film composites. b) Relationship of electrical resistance and strain along two orthogonal directions under initial loading. c-d) Tensile snapshots of samples at different strains under initial loading. e-f) Relationship of electrical resistance and strain along two orthogonal directions under cyclic loading. g-h) Tensile snapshots of samples at different strains under 4th loading cycle. (i) Schematic for the formation of crakcs and effect mechanisms on resistance responses along (‖) and (⊥) directions.

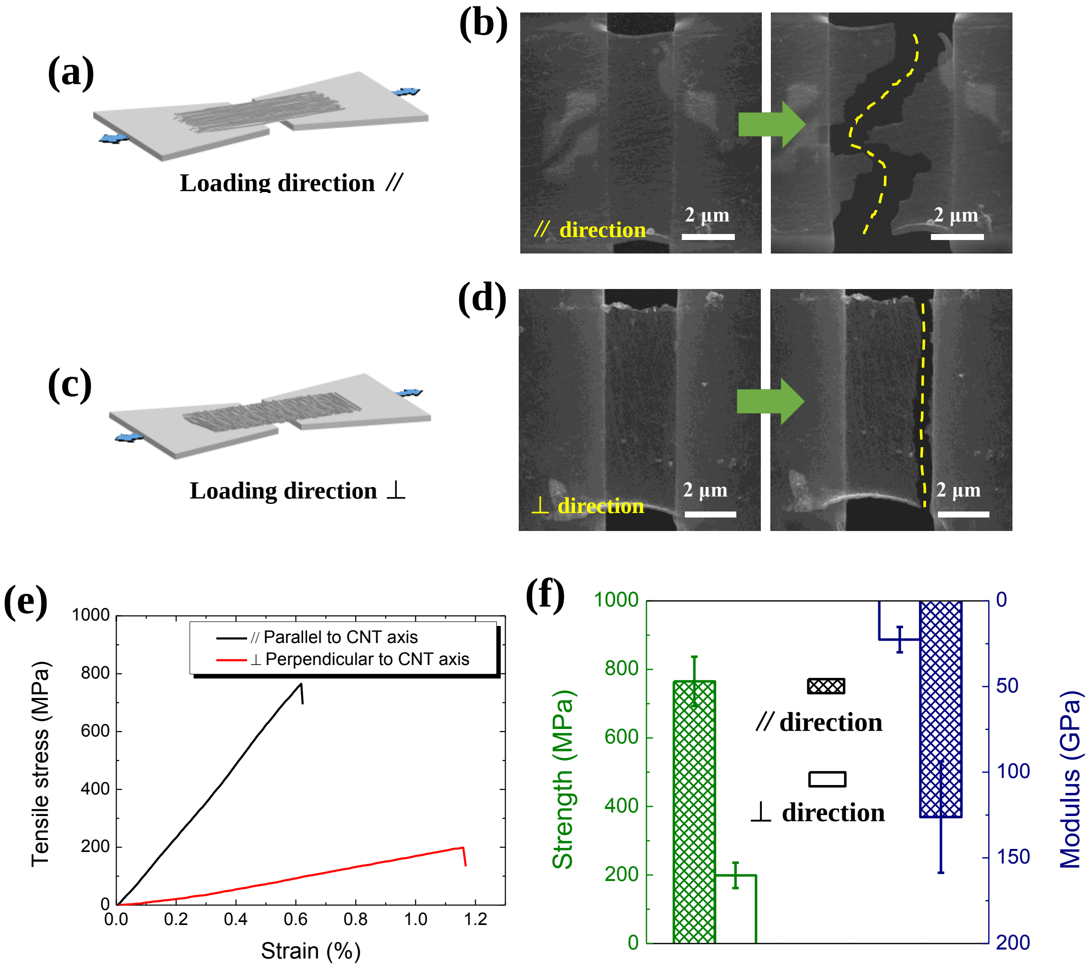

Fig. 3. In situ tension of SWCNT films. a) Schematic for in situ tensile testing along ∥ direction, where ∥ means that the tensile direction is parallel to axial direction of CNTs. b) SEM images for SWCNT films before and after loading along ∥ direction. c) Schematic for in situ tensile testing along ⊥ direction, where ⊥ means that the tensile direction is perpendicular to axial direction of CNTs. d) SEM images for SWCNT films before and after loading along ⊥ direction. e) Tensile stress-strain curves of a SWCNT film along ∥ and ⊥ directions. f) Comparison of tensile strength and young’s modulus along two directions.

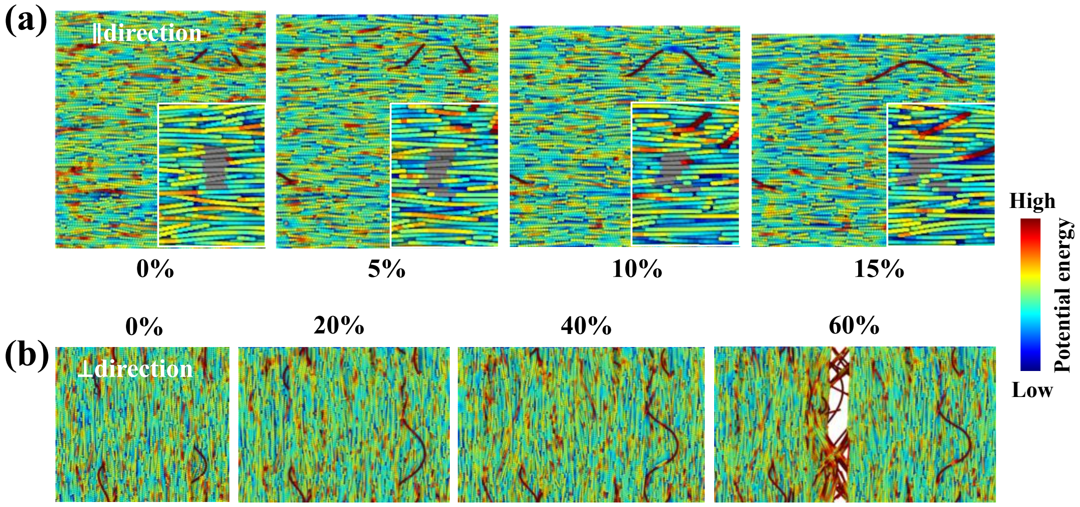

Fig. 4. CGMD simulations of SWCNT films along two directions under tensile loading. a) Structural evolvement of SWCNT film along ‖ direction. Strain-induced sliding failure was clearly identified by tracking the target sidewall contact between as shown in the insets. b) Structural evolvement of SWCNT film along ⊥ direction. The peeling failure can result in a bridging at cracks.

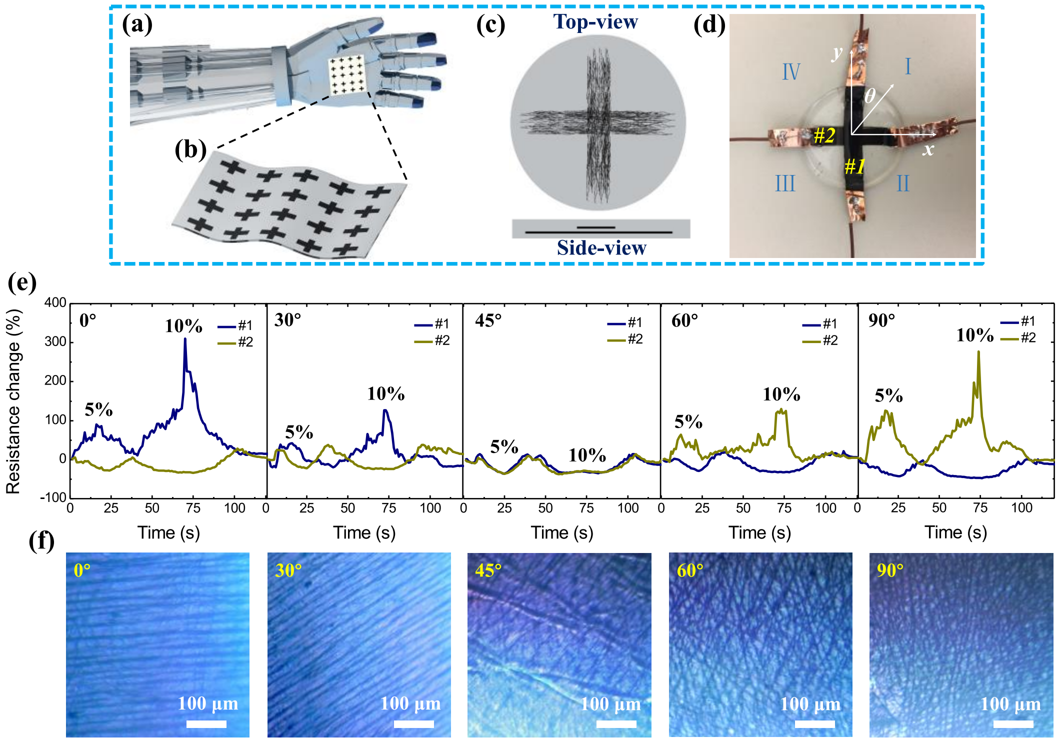

Fig. 5. Direction-sensitive artificial skins for robots. a) A schematic for a robot arm, where a piece of artificial skin was covered on the arm of a robot. b) Schematic of direction-sensitive artificial skins. c) Schematic top and side views of a cross-like laminated structure assembled by two aligned SWCNT films. d) Image of a piece of prepared direction-sensitive artificial skin. e) Response of electrical signal to loading and unloading with different strains. f) Images of samples under the tensile loading along different angle θ.